

Supporting Information

Direct Determination of Multiphoton Absorption Cross-Sections by Transient Absorption Spectroscopy

Huajun He, Jia Wei Melvin Lim, Minjun Feng, Zengshan Xing and Tze Chien Sum*

Division of Physics and Applied Physics, School of Physical and Mathematical Sciences, Nanyang Technological University, 21 Nanyang Link, Singapore 637371, Singapore.

* Corresponding author

Tze Chien Sum: Tzechien@ntu.edu.sg

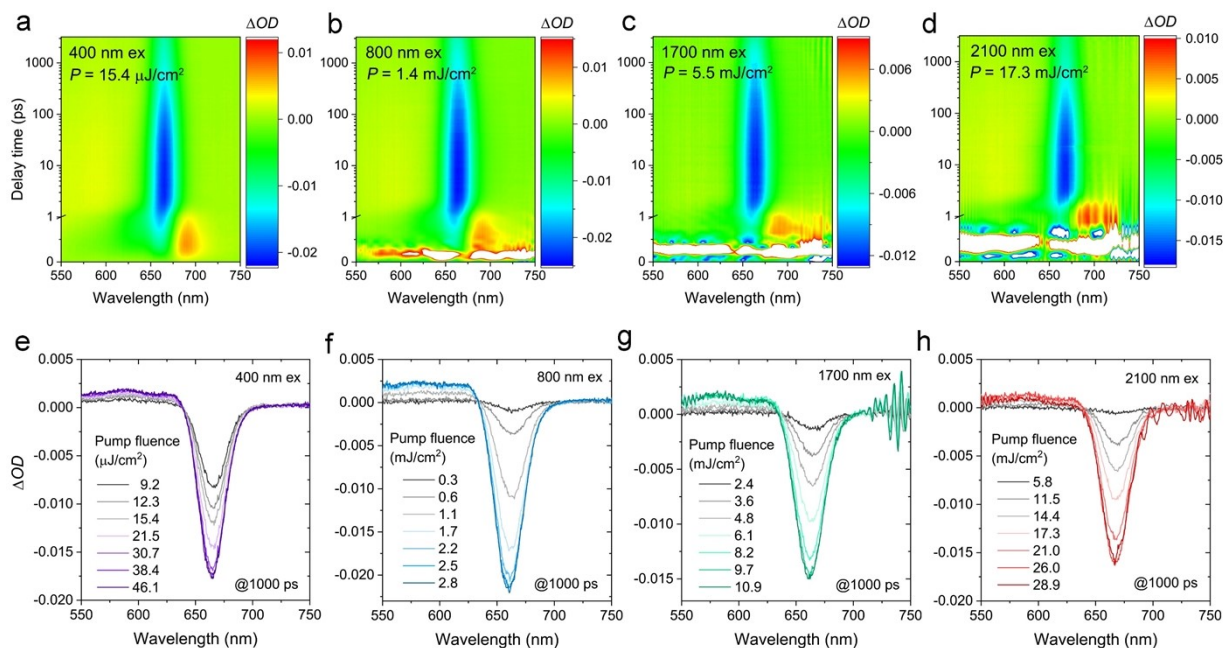


Figure S1. TA analysis of the photobleaching signal of CsPbI₃ NCs. (a-d) Pseudo-colour TA contour plots with excitation wavelength at 400 nm (1PE, a), 800 nm (2PE, b), 1700 nm (3PE, c) and 2100 nm (4PE, d). (e-h) Pump fluence dependent TA spectra in the region of bleaching signal at the delay time of 1,000 ps, with excitation wavelength at 400 nm (e), 800 nm (f), 1700 nm (g), and 2100 nm (h).

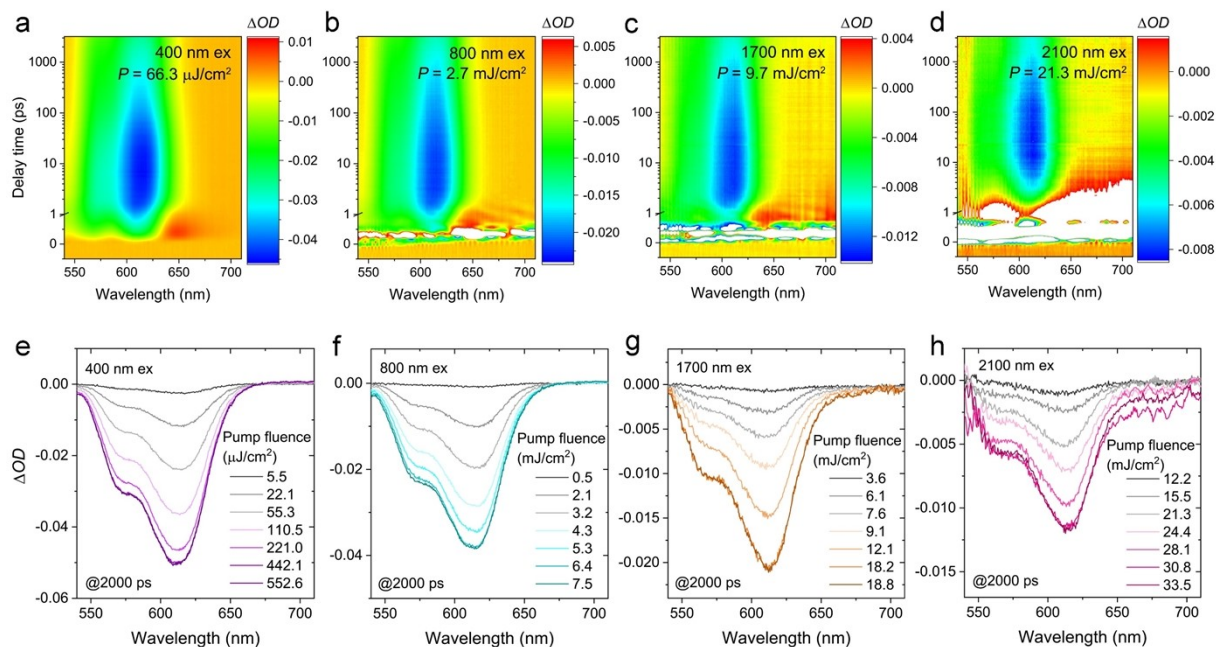


Figure S2. TA analysis of the photobleaching signal of CdSe/ZnS QDs. (a-d) Pseudo-colour TA contour plots with excitation wavelength at 400 nm (1PE, a), 800 nm (2PE, b), 1700 nm (3PE, c) and 2100 nm (4PE, d). (e-h) Pump fluence dependent TA spectra in the region of bleaching signal at the delay time of 2000 ps, with excitation wavelength at 400 nm (e), 800 nm (f), 1700 nm (g), and 2100 nm (h).

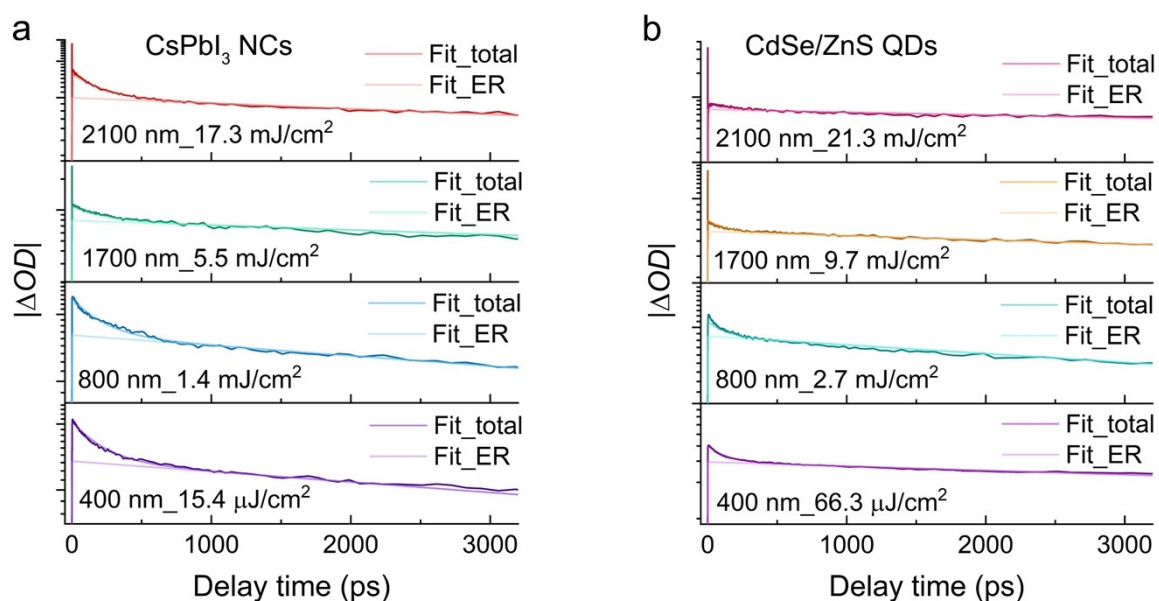


Figure S3. TA decay kinetics at the photobleaching signal of CsPbI₃ NCs and CdSe/ZnS QDs samples. (a) TA kinetics at the bleaching signal of CsPbI₃ NCs with excitation wavelength of 400 nm, 800 nm, 1700 nm and 2100 nm, which leave only TA signals reflecting the single exciton participation under the long pump-probe delay time >800 ps. (b) TA kinetics at the bleaching signal of CdSe/ZnS QDs with excitation wavelength of 400 nm, 800 nm, 1700 nm and 2100 nm, which leave only TA signals reflecting the single exciton participation under the long pump-probe delay time >400 ps. ER: exciton recombination. Detailed fitting parameters for TA decay kinetics are shown in **Table S3**.

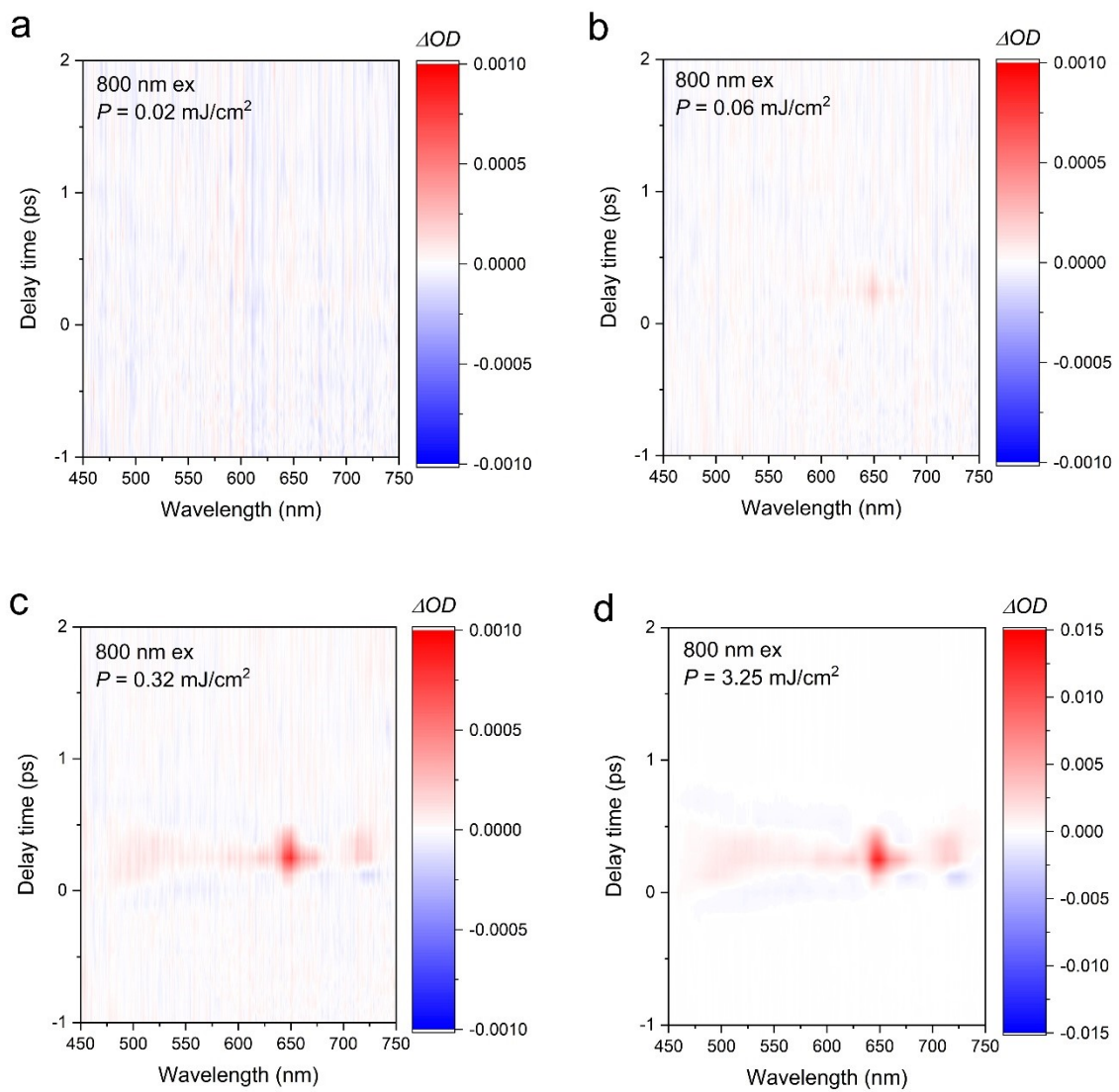


Figure S4. The cross correlation between the 800 nm pulse and the white light (WL) pulse. (a-d) The cross-correlation investigation at different pump fluence (P) are presented in panel (a), (b), (c) and (d), respectively. The cross-correlation signal is detectable even at a low pump fluence of only ~ 0.06 mJ/cm².

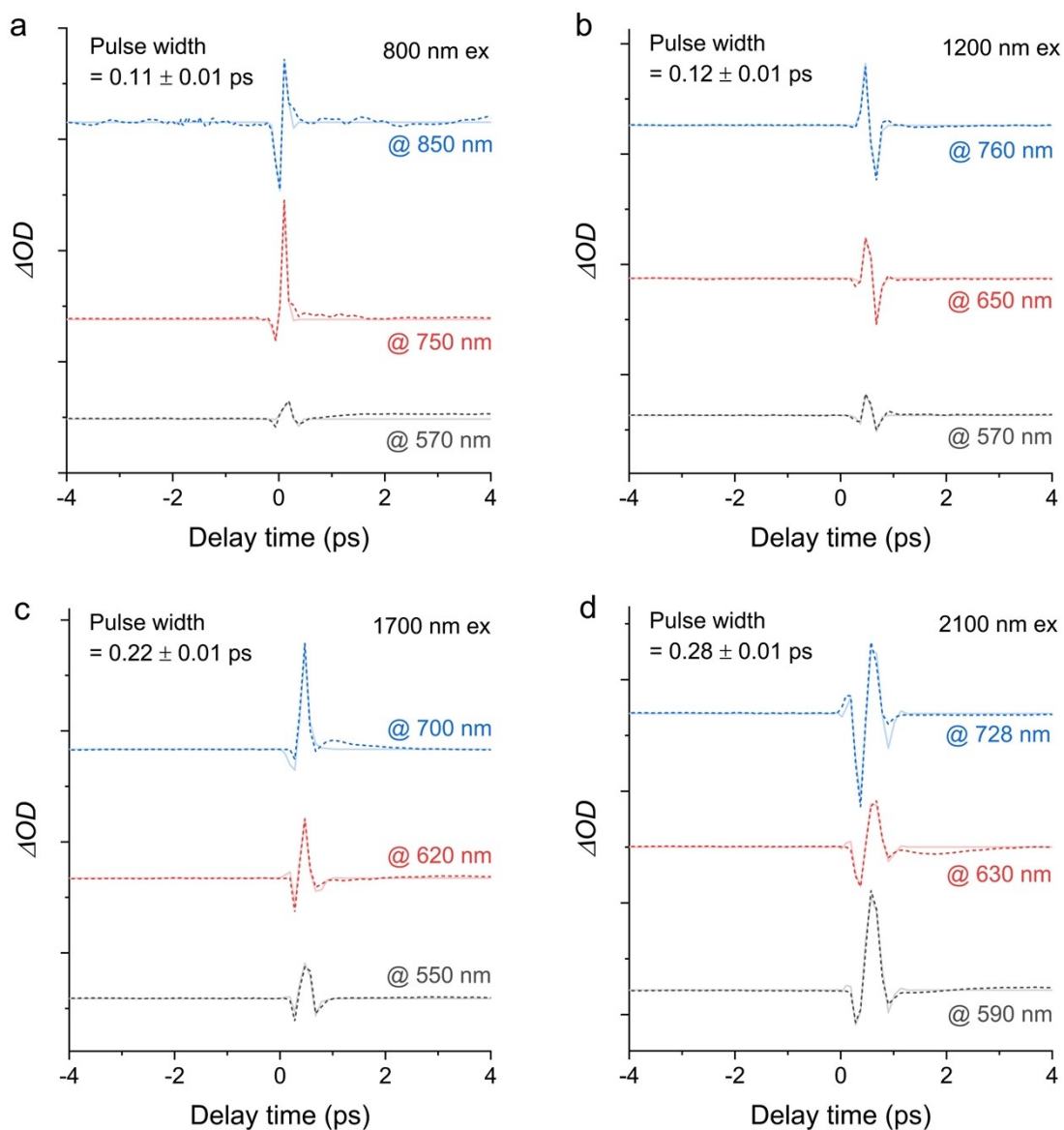


Figure S5. Pulse width of the pump derived from the cross correlation between the infrared pulse and the white light (WL) pulse. (a-d) The cross correlation of 800 nm, 1200 nm, 1700 nm and 2100 nm infrared pulse with WL pulse at representative wavelengths are presented in panel (a), (b), (c) and (d), respectively. The plots show the experimental data (dashed line) and non-resonant response global fitting (solid line). The fitting method is discussed in the supplementary notes below.

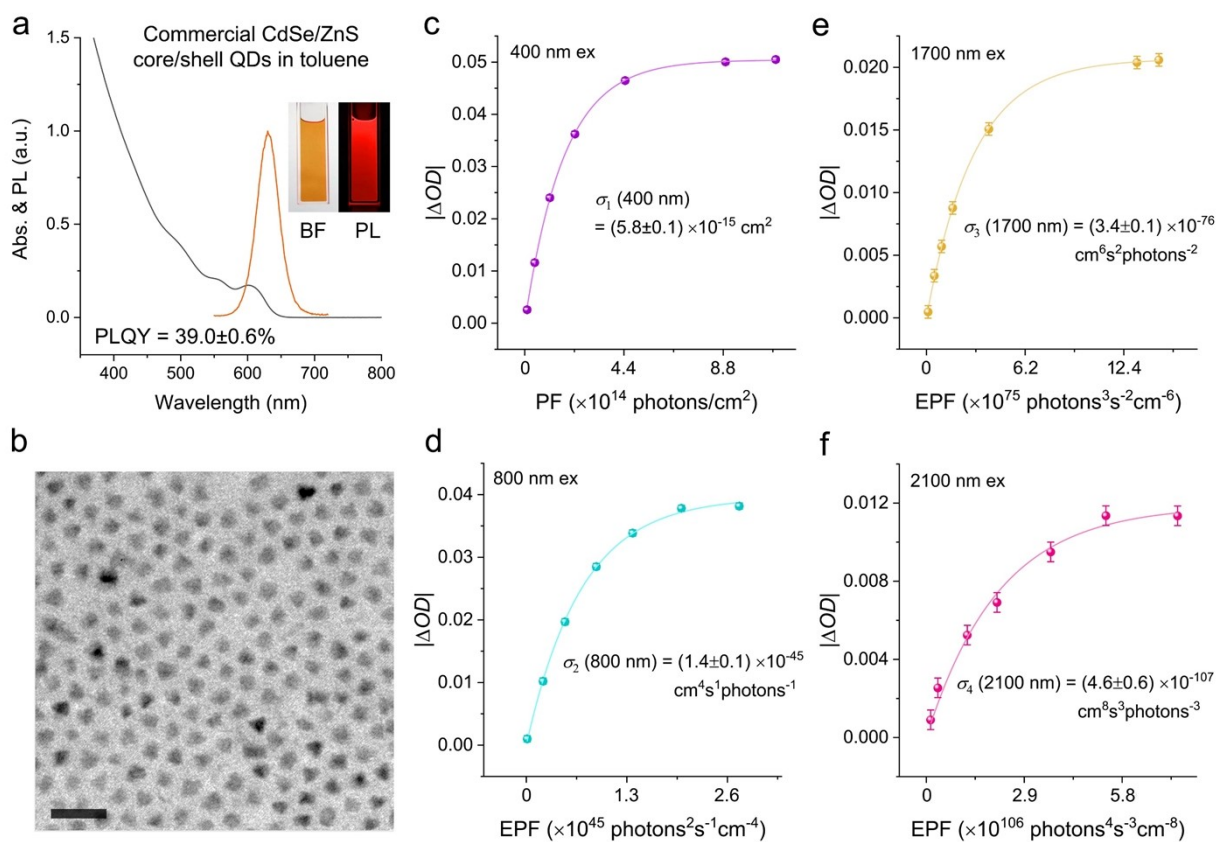


Figure S6. Single-photon and multi-photon absorption cross-sections of commercial CdSe/ZnS core/shell QDs. (a) Absorption and PL spectra of CdSe/ZnS QDs in toluene. Insets: images of CdSe/ZnS QDs in toluene under BF and 365 nm excitation. (b) TEM images of CdSe/ZnS QDs, showing the average size is ~ 5 nm. Scale bar, 20 nm. (c-f) $|\Delta OD|$ as the function of photon fluence (PF) for 400 nm excitation (c) or equivalent photon fluence (EPF) for multiphoton excitation (800 nm in (d), 1700 nm in (e) and 2100 nm in (f) at the delay time of 2,000 ps. The solid curves are the best fit to **Equation (1)** in main text, which are used derive linear/nonlinear absorption cross-sections.

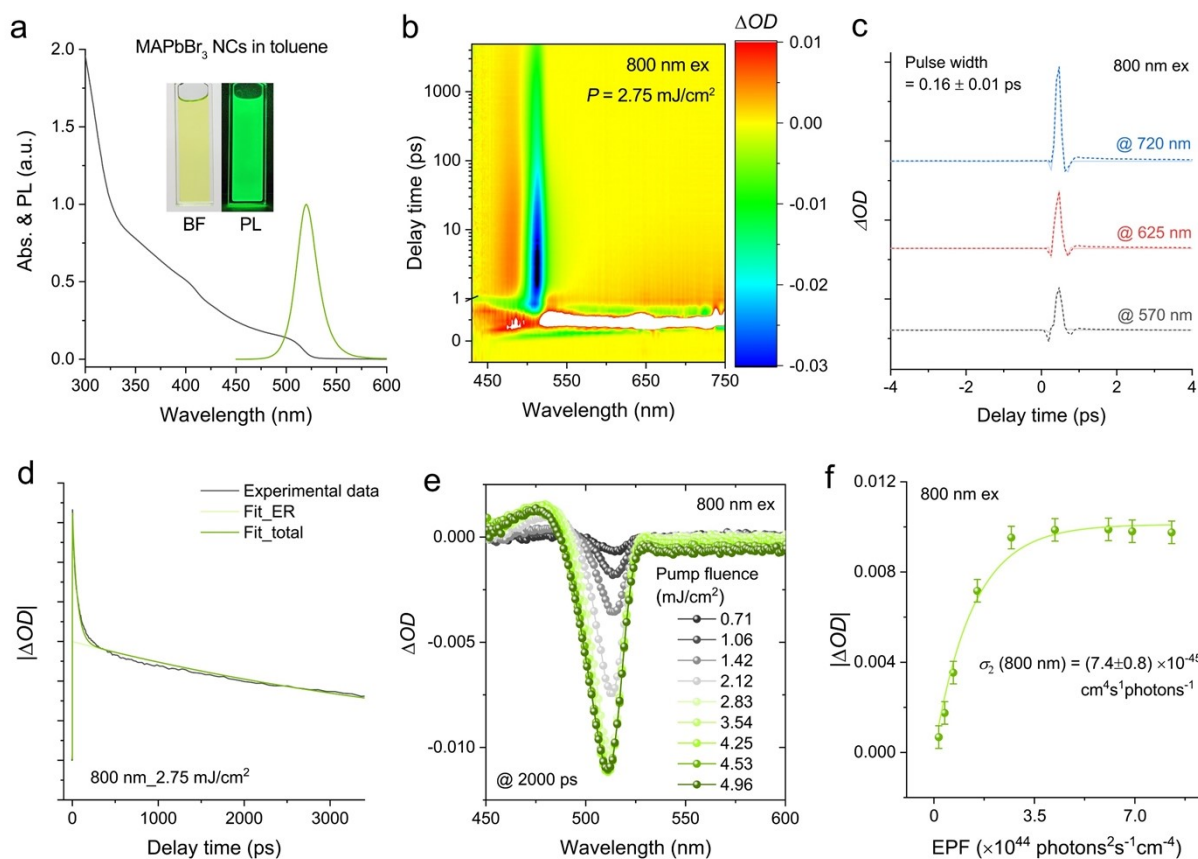


Figure S7. Two-photon absorption cross-section measurements of MAPbBr₃ NCs. (a) Absorption and photoluminescence (PL) spectra of MAPbBr₃ NCs in toluene. Inset: images of MAPbBr₃ NCs in toluene under bright field (BF) and 365 nm excitation. (b) Pseudo-colour TA contour plots with excitation wavelength at 800 nm. (c) The cross correlation of 800 nm infrared pulse with WL pulse at representative wavelengths, deriving the pulse width of 800 nm pump signal to be ~160 fs. (d) TA kinetics at the bleaching signal with excitation wavelength of 800 nm, which leaves only TA signal reflecting the single exciton participation under the long pump-probe delay time >300 ps. ER: exciton recombination. (e) Pump fluence dependent TA spectra in the region of bleaching signal at the delay time of 2000 ps, with excitation wavelength at 800 nm. (f) $|\Delta OD|$ as the function of equivalent photon fluence (EPF) for 2-photon excitation (800 nm) at the delay time of 2000 ps. The solid curves are the best fit to **Equation (1)** in main text, which are used to derive the 2-photon absorption cross-section.

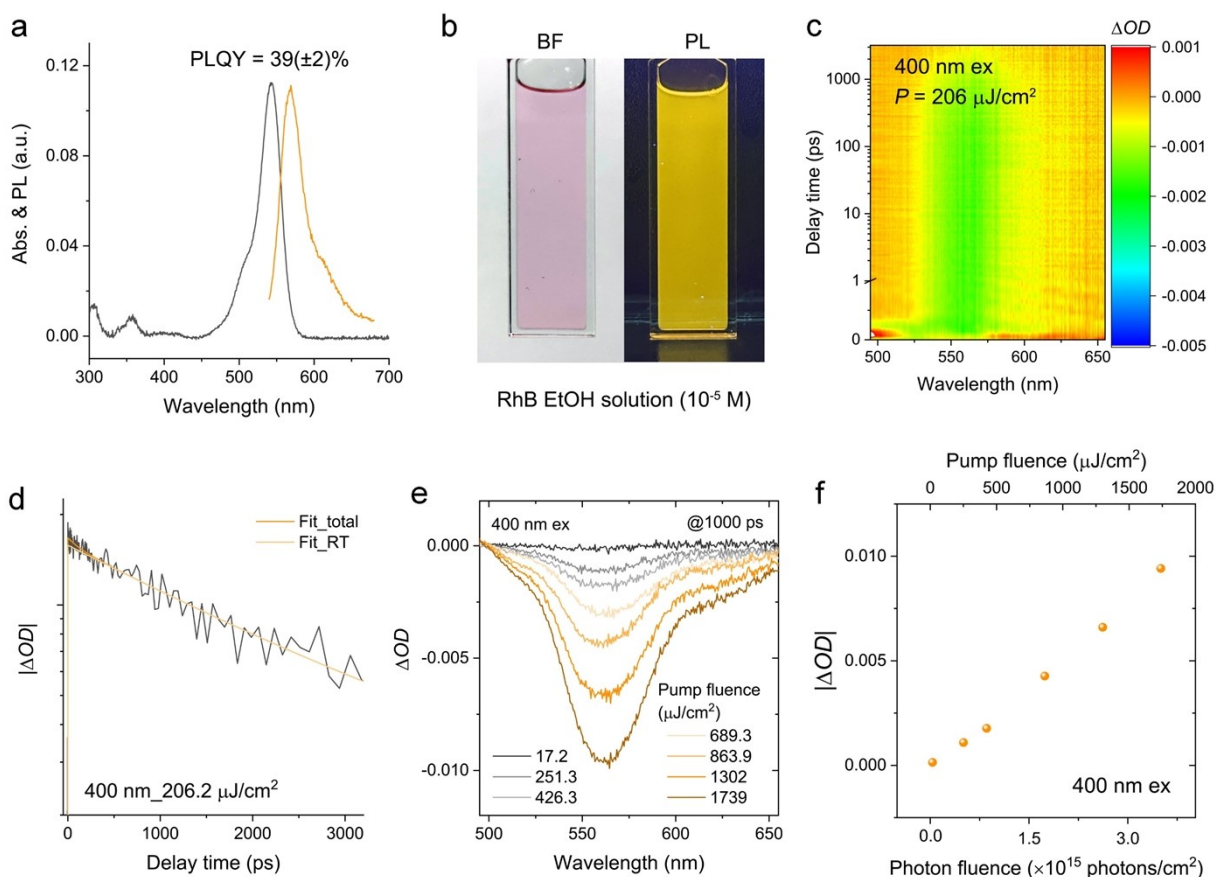


Figure S8. Basic optical spectra and TA analysis of the photobleaching signal of Rhodamine B (RhB) ethanol solution. (a) Absorption and PL spectra of RhB ethanol solution with concentration of 10^{-5} M. (b) Images of RhB ethanol solution under BF and 365 nm excitation. (c) Pseudo-colour TA contour plots with excitation wavelength at 400 nm. (d) TA kinetics at the bleaching signal with excitation wavelength of 400 nm, which leaves only TA signal reflecting the single exciton participation under the long pump-probe delay time >300 ps. RT: radiation transition. (e) TA spectra in the region of bleaching signal at the delay time of 1000 ps, with excitation wavelength at 400 nm. (f) Photon fluence dependent $|\Delta OD|$ plots under 400 nm excitation at the delay time of 1000 ps. $|\Delta OD|$ has not reached saturation even at extremely high pump fluence of >1.7 mJ/cm², due to weak sample absorption at 400 nm.

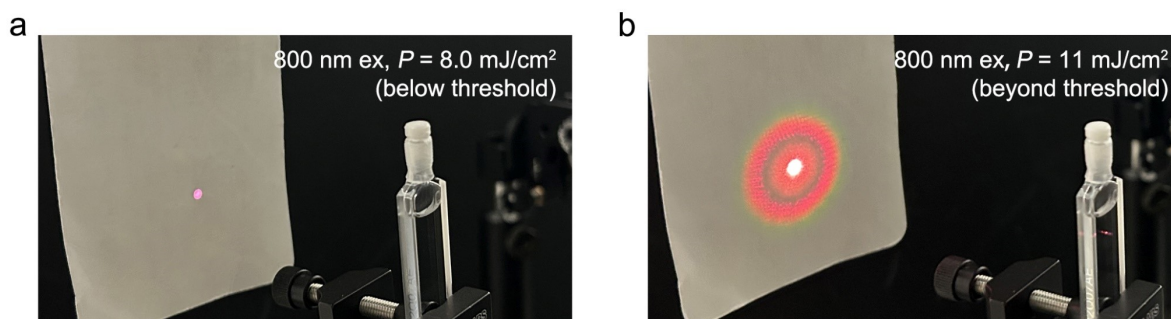


Figure S9. Non-linear optical generation process of the quartz cuvette upon excitation of 800 nm. (a-b) Images of the quartz cuvette (containing toluene) under 800 nm excitation with pump fluence below (a)/beyond (b) the threshold of ~ 10.2 mJ/cm². No filter was placed behind the cuvette.

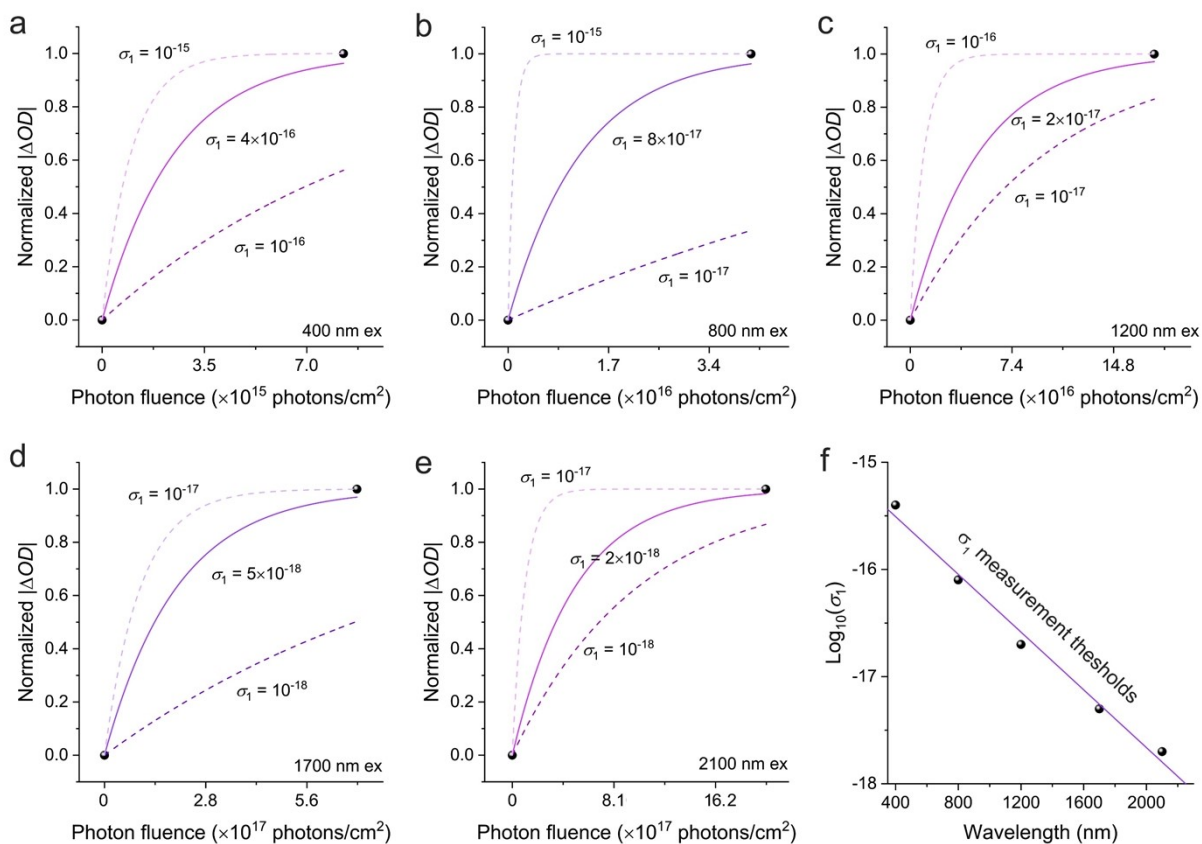


Figure S10. Simulated fitting for single-photon excitation. (a-e) The solid curves are fitted by Equation 1 in main text with different σ_1 upon representative excitation of 400 nm (a), 800 nm (b), 1200 nm (c), 1700 nm (d) and 2100 nm (e), respectively. The parameter a is set to be unity for the normalized $|\Delta OD|$. For the excitation pump fluence limit from 400 nm to 2100 nm shown in **Figure 4c** in the main text, the minimum measurable values of σ_1 at 400 nm to 2100 nm by the system are shown in solid lines in panels (a-e). Assuming the measured $|\Delta OD|$ reaches saturation (normalized to unity) at the pump fluence limit and constrain the difference between the fitted $|\Delta OD|$ value at that limit and the ideal saturated value (*i.e.*, unity) to within 0.05 (based on the measurement error). (f) Wavelength dependent σ_1 measurement thresholds of the system. Unit of σ_1 : cm^2 .

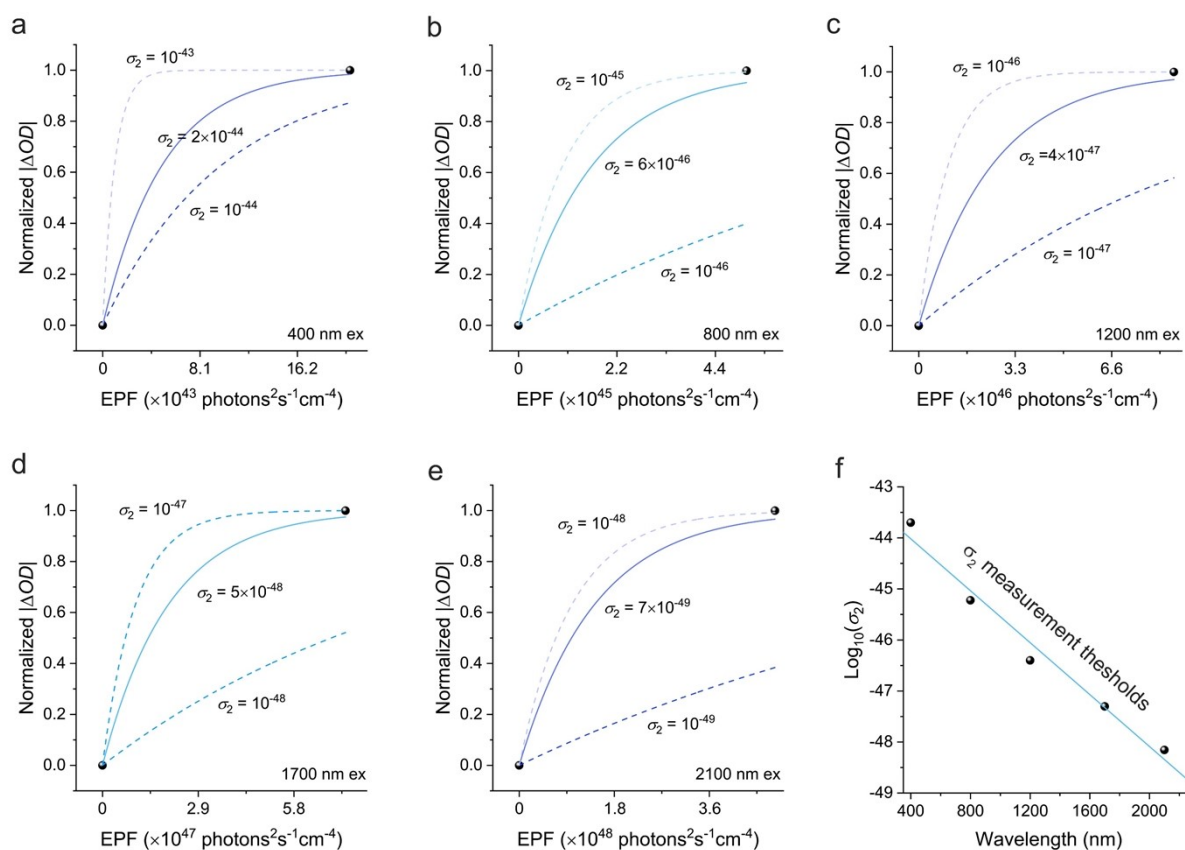


Figure S11. Simulated fitting for two-photon excitation. (a-e) The solid curves are fitted by Equation 1 in main text with different σ_2 upon representative excitation of 400 nm (a), 800 nm (b), 1200 nm (c), 1700 nm (d) and 2100 nm (e), respectively. The parameter a is set to be unity for the normalized $|\Delta OD|$. The pump pulse width values are set according to the **Figure S4**, and assuming that the 400 nm pump possesses the same pulse width with that of 800 nm pump. For the excitation pump fluence limit from 400 nm to 2100 nm shown in **Figure 4c** in the main text, the minimum measurable values of σ_2 at 400 nm to 2100 nm by the system are shown in solid lines in panels (a-e). Assuming the measured $|\Delta OD|$ reaches saturation (normalized to 1) at the pump fluence limit and constrain the difference between the fitted $|\Delta OD|$ value at that limit and the ideal saturated value (*i.e.*, unity) to within 0.05 (based on the measurement error). (f) Wavelength dependent σ_2 measurement thresholds of the system. EPF: Equivalent photon fluence. Unit of σ_2 : $\text{cm}^4\text{s}^{-1}\text{photons}^{-1}$.

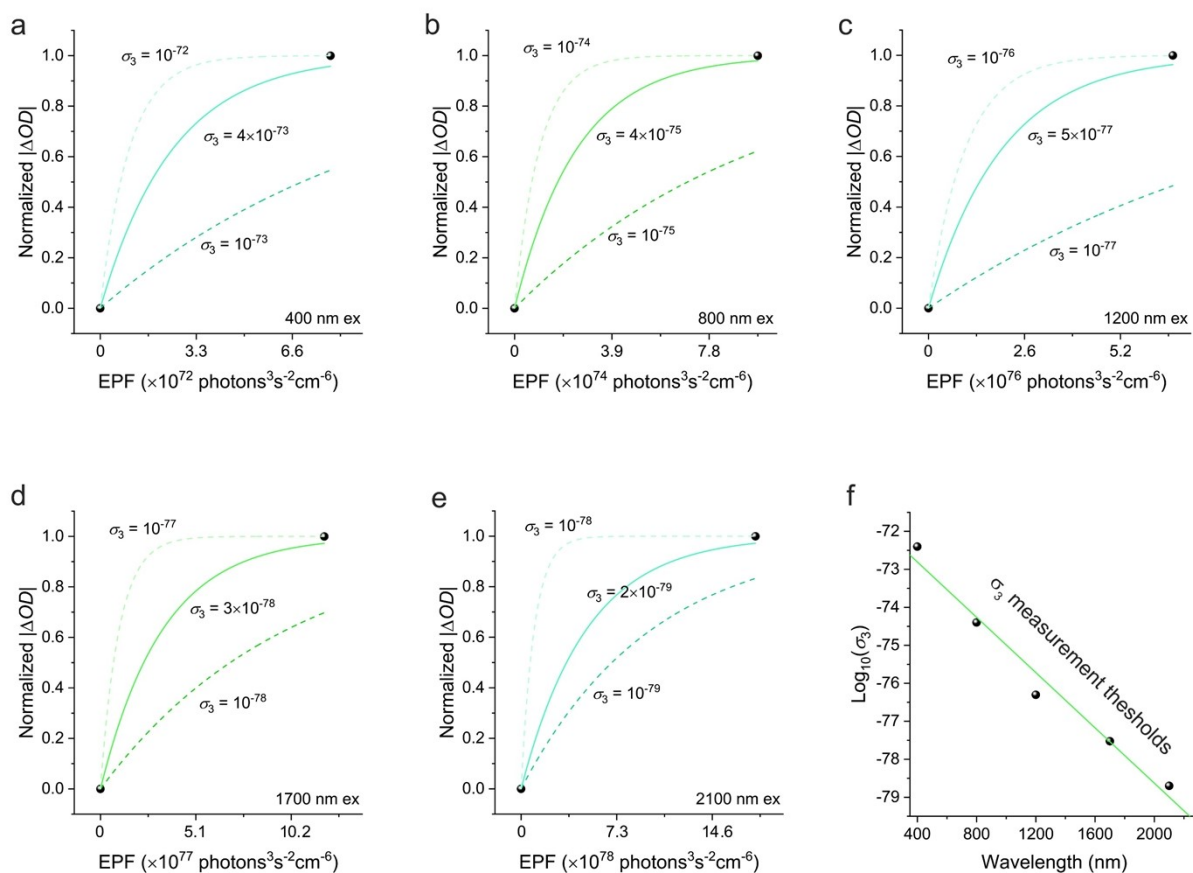


Figure S12. Simulated fitting for three-photon excitation. (a-e) The solid curves are fitted by Equation 1 in main text with different σ_3 upon representative excitation of 400 nm (a), 800 nm (b), 1200 nm (c), 1700 nm (d) and 2100 nm (e), respectively. The parameter a is set to be unity for the normalized $|\Delta OD|$. The pump pulse width values are set according to the **Figure S4**, and assuming that the 400 nm pump possesses the same pulse width with that of 800 nm pump. For the excitation pump fluence limit from 400 nm to 2100 nm shown in **Figure 4c** in the main text, the minimum measurable values of σ_3 at 400 nm to 2100 nm by the system are shown in solid lines in panels (a-e). Assuming the measured $|\Delta OD|$ reaches saturation (normalized to unity) at the pump fluence limit and constrain the difference between the fitted $|\Delta OD|$ value at that limit and the ideal saturated value (*i.e.*, unity) to within 0.05 (based on the measurement error). (f) Wavelength dependent σ_3 measurement thresholds of the system. EPF: Equivalent photon fluence. Unit of σ_3 : $\text{cm}^6\text{s}^2\text{photons}^{-2}$.

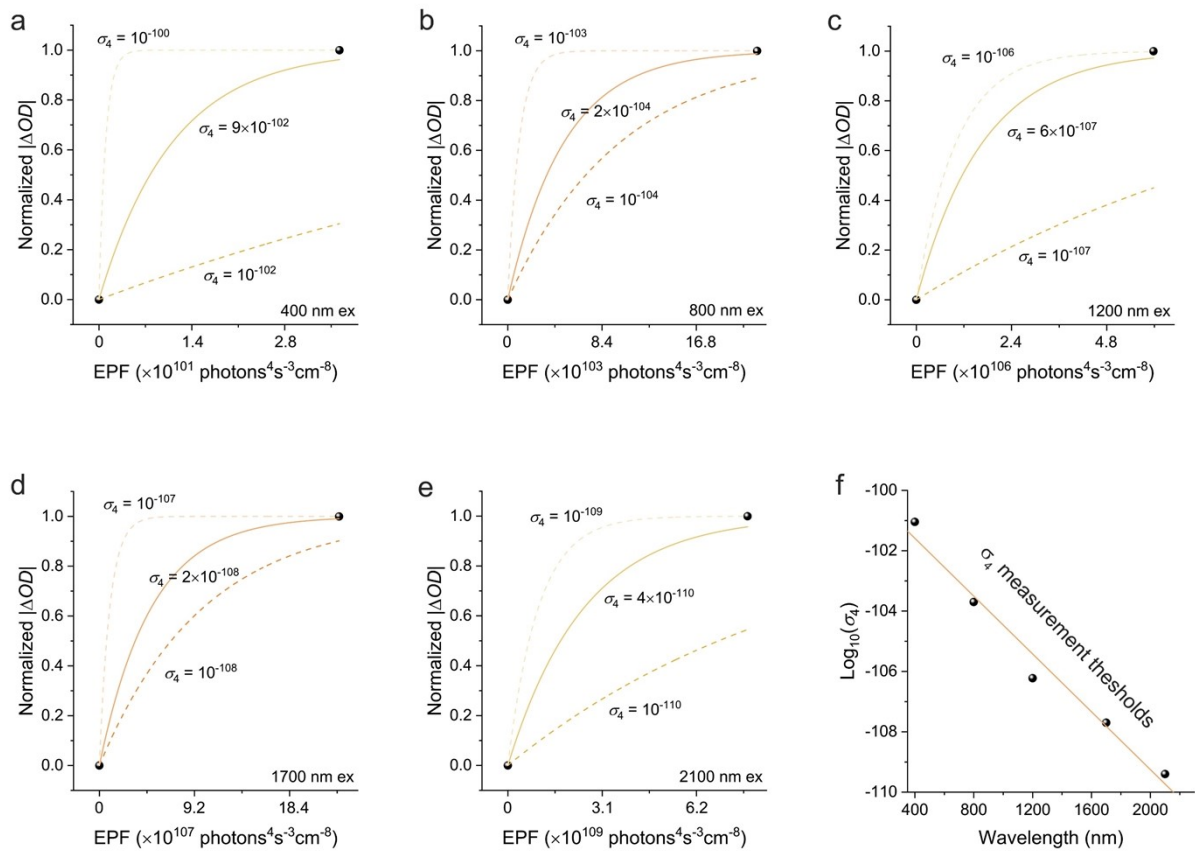


Figure S13. Simulated fitting for four-photon excitation. (a-e) The solid curves are fitted by Equation 1 in main text with different σ_4 upon representative excitation of 400 nm (a), 800 nm (b), 1200 nm (c), 1700 nm (d) and 2100 nm (e), respectively. The parameter a is set to be unity for the normalized $|\Delta OD|$. The pump pulse width values are set according to the **Figure S4**, and assuming that the 400 nm pump possesses the same pulse width with that of 800 nm pump. For the excitation pump fluence limit from 400 nm to 2100 nm shown in **Figure 4c** in the main text, the minimum measurable values of σ_4 at 400 nm to 2100 nm by the system are shown in solid lines in panels (a-e). Assuming the measured $|\Delta OD|$ reaches saturation (normalized to unity) at the pump fluence limit and constrain the difference between the fitted $|\Delta OD|$ value at that limit and the ideal saturated value (*i.e.*, unity) to within 0.05 (based on the measurement error). (f) Wavelength dependent σ_4 measurement thresholds of the system. EPF: Equivalent photon fluence. Unit of σ_4 : $\text{cm}^8\text{s}^3\text{photons}^{-3}$.

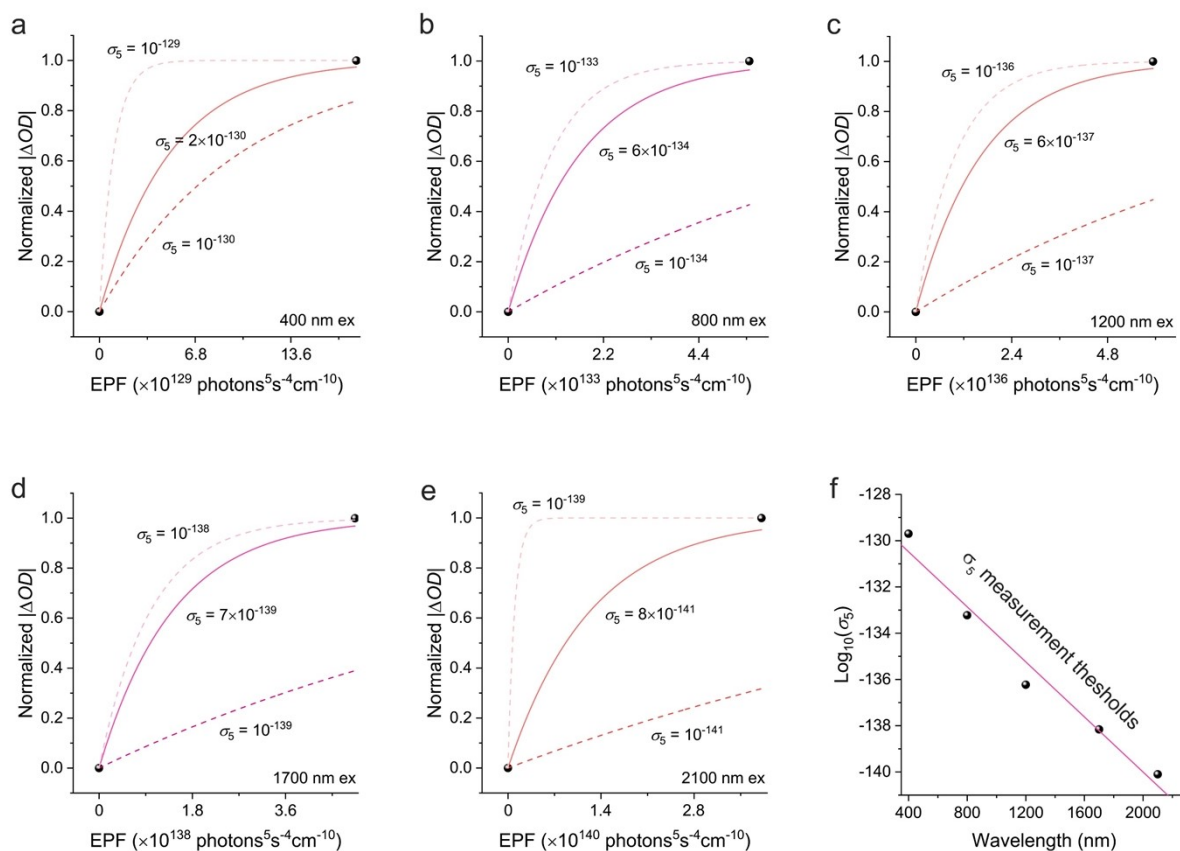


Figure S14. Simulated fitting for five-photon excitation. (a-e) The solid curves are fitted by Equation 1 in main text with different σ_5 upon representative excitation of 400 nm (a), 800 nm (b), 1200 nm (c), 1700 nm (d) and 2100 nm (e), respectively. The parameter a is set to be unity for the normalized $|\Delta OD|$. The pump pulse width values are set according to the **Figure S4**, and assuming that the 400 nm pump possesses the same pulse width with that of 800 nm pump. For the excitation pump fluence limit from 400 nm to 2100 nm shown in **Figure 4c** in the main text, the minimum measurable values of σ_5 at 400 nm to 2100 nm by the system are shown in solid lines in panels (a-e). Assuming the measured $|\Delta OD|$ reaches saturation (normalized to unity) at the pump fluence limit and constrain the difference between the fitted $|\Delta OD|$ value at that limit and the ideal saturated value (*i.e.*, unity) to within 0.05 (based on the measurement error). (f) Wavelength dependent σ_5 measurement thresholds of the system. EPF: Equivalent photon fluence. Unit of σ_5 : $\text{cm}^{10}\text{s}^4\text{photons}^{-4}$.

Table S1. MACSs (σ_n) of state-of-the-art MPA micro/nano materials.

Materials	λ_{em} (nm)	η (%)	σ_2 ($\times 10^5$ GM)	σ_3 ($\times 10^{-78}$ cm ⁶ s ² photon ⁻²)	σ_4 ($\times 10^{-110}$ cm ⁸ s ³ photon ⁻³)	σ_5 ($\times 10^{-140}$ cm ¹⁰ s ⁴ photon ⁻⁴)
Organic conjugated molecule SpL-3 ¹	~480	86	0.09 (745 nm)	2.39 $\times 10^4$ (940 nm)	5.1 $\times 10^3$ (1440 nm)	9.3 $\times 10^3$ (1540 nm)
Metallo dendrimer 3G _{22,03,02,01} -s ²	N.A.	N.A.	1.1 (700 nm)	230 (1250 nm)	7.3 $\times 10^3$ (1650 nm)	500 (2050 nm)
AIE DCBT dots ³	642	13.6	N.A.	5.61 (1550 nm)	N.A.	N.A.
AIE TPAPhCN dots ⁴	645	26	18.5 (900 nm)	2.45 $\times 10^5$ (1200 nm)	N.A.	N.A.
(MOF) Zr/CO ₂ CF ₃ /TCPE _{kagome} ⁵	~480	N.A.	≥ 0.036 (600 nm)	≥ 15 (990 nm)	≥ 400 (1440 nm)	N.A.
(MOF \supset PNCs) ZJU-28 \supset MAPbBr ₃ ⁶	530	51.1	23 (960 nm)	1.4 $\times 10^4$ (1440 nm)	2.7 $\times 10^5$ (1800 nm)	5.3 $\times 10^4$ (2100 nm)
MAPbBr ₃ NCs in toluene ⁷	~520	84	4.8-62 (675-1000 nm)	3.9 $\times 10^3$ -3.3 $\times 10^4$ (1050-1500 nm)	4.2 $\times 10^4$ -3.6 $\times 10^6$ (1550-2000 nm)	460-2.9 $\times 10^4$ (2050-2300 nm)
CsPbBr ₃ NCs in toluene ⁷	518	55	18-240 (675-1000 nm)	7 $\times 10^3$ -1.4 $\times 10^5$ (1050-1500 nm)	1.3 $\times 10^5$ -1.3 $\times 10^7$ (1550-2000 nm)	1.7 $\times 10^3$ -1.2 $\times 10^5$ (2050-2300 nm)
MAPbBr ₃ /(OA) ₂ PbBr ₄ NCs in toluene ⁷	~520	92	33-400 (675-1000 nm)	2.7 $\times 10^4$ -2.4 $\times 10^5$ (1050-1500 nm)	2.3 $\times 10^5$ -2.6 $\times 10^7$ (1550-2000 nm)	3.1 $\times 10^3$ -2.2 $\times 10^5$ (2050-2300 nm)
CdSe/CdS nanorod ⁸	570-590	32-61	N.A.	590-1.5 $\times 10^3$ (1300 nm)	N.A.	N.A.
Surfactant-capped CdS QDs ⁹	~480	N.A.	10 (532 nm)	8 $\times 10^5$ (1064 nm)	N.A.	N.A.
ZnSe and ZnSe/Zns QDs ¹⁰	N.A.	N.A.	N.A.	1.2 $\times 10^3$ -2.4 $\times 10^3$ (1064 nm)	N.A.	N.A.
Commercial Qtracker800 ¹¹	~800	≥ 26	N.A.	≤ 6.46 (2200 nm)	N.A.	N.A.
Commercial Qtracker655 ¹¹	~655	≥ 44	N.A.	N.A.	$\leq 1.8 \times 10^3$ (2200 nm)	N.A.
Commercial CdSe/ZnS QDs in toluene (this work)	630	39	1.4 (800 nm)	340 (1700 nm)	4.6 $\times 10^3$ (2100 nm)	N.A.
CsPbI ₃ NCs in toluene (this work)	682	94	11.5 (800 nm)	2.5 $\times 10^3$ (1700 nm)	2.1 $\times 10^4$ (2100 nm)	N.A.

λ_{em} : emission centre wavelength; η : photoluminescence quantum yield (PLQY)

Table S2. Linear absorption cross-sections (σ_1) of representative QDs/NCs.

Materials	λ_{em} (nm)	σ_1 ($\times 10^{-15}$ cm ²)
CdSe QDs (3-6 nm) ¹²	N.A.	1.8-15 (350 nm)
CdTe QDs (2-8 nm) ¹³	N.A.	0.34-22 (400 nm)
InP NCs (2.8-5.2 nm) ¹⁴	~610-760	2.8-20 (350 nm)
PbS QDs (3.6-6.5 nm) ¹⁵	N.A.	3.8-24 (400 nm)
CsPbCl ₃ NCs (~9.8 nm) ¹⁶	409 nm	43 (350 nm)
CsPbBr ₃ NCs (3.8-6.9 nm) ¹⁷	N.A.	4.5-32 (400 nm)
CsPbBr ₃ NCs (6.3-9.3 nm) ¹⁸	487-511	3.5-13 (400 nm)
CsPbI ₃ NCs (11.2 nm) ¹⁸	683	13 (400 nm)
Commercial CdSe/ZnS QDs in toluene (~5 nm, this work)	630	5.8 (400 nm)
CsPbI ₃ NCs in toluene (~10 nm, this work)	682	33 (400 nm)

λ_{em} : emission centre wavelength.

Table S3. Fitted parameters for TA delay curves.

Materials	Excitation wavelength	Fitted parameters			
		$A_1 (\times 10^{-4})$	$A_2 (\times 10^{-4})$	τ_1 (ns)*	τ_2 (ns)#
CsPbI ₃ NCs (~10 nm)	400 nm	71 ± 4	140 ± 5	0.21 ± 0.02	9 ± 1
	800 nm	76 ± 4	162 ± 4		
	1700 nm	31 ± 3	78 ± 3		
	2100 nm	58 ± 3	99 ± 3		
Commercial CdSe/ZnS core/shell QDs (~5 nm)	400 nm	120 ± 6	328 ± 7	0.13 ± 0.02	12 ± 2
	800 nm	26 ± 5	183 ± 5		
	1700 nm	25 ± 4	105 ± 4		
	2100 nm	15 ± 8	67 ± 5		

*Global fitted data; τ_1 : Auger recombination

#Global fitted data; τ_2 : Exciton recombination.

Supplementary Notes

1. Experimental Sections

Materials. Lead iodide (99.999%), cesium acetate (CsOAc, 99.9%), oleylamine (OAm, 70%), oleic acid (OAc, 90%), methyl acetate (MeOAc, anhydrous, 99.5%), toluene (anhydrous, 99.8%), 1-octadecene (ODE, 90%), ethanol (anhydrous, $\geq 99.5\%$), Rhodamine B ($\geq 95\%$), were purchased from Sigma-Aldrich (St. Louis, Missouri, USA). CdSe/ZnS core/shell QDs were purchased from Evident Technologies, Inc. (Troy, New York, USA). Reagents were used as such unless until mentioned further purification.

Synthesis of CsPbI₃ NCs. CsPbI₃ nanocrystals were synthesized according to the reported traditional hot injection method.¹⁹ All the procedures were performed with a standard Schlenk line. The Cs-Oleate precursor was prepared by first degassing 157.8 mg of CsOAc along with 0.5 mL of OAc in 5 mL of ODE in a round bottom flask at 100 °C under vacuum for 30 min with vigorous stirring. Following, the flask was kept under nitrogen flow and the temperature was raised to 120 °C. The resulting pale-yellow Cs-Oleate solution was kept at 120 °C prior to injection. To prepare the nanocrystals, 86.7 mg of PbI₂, 0.5 mL of OAc and 0.5 mL of OAm along with 5 mL of ODE were first similarly degassed for 30 min at 100 °C. Then, the flask was kept under nitrogen flow and the temperature increased to 160 °C and maintained for a while until the temperature stabilized. 0.4 mL of the Cs-oleate solution was then injected and the solution rapidly turned dark brown. The reaction was quenched after ~5 seconds by immersing the flask in an ice water bath. To purify the crude NCs, MeOAc was added to the crude solution in a 2:1 ratio and centrifuged at 8,000 rpm. The supernatant was discarded while the precipitate was redispersed in toluene and centrifuged again at 4,000 rpm to discard the large particles. The final supernatant was then kept in a refrigerator for further use.

Measurements. For single-/multi-photon excited femtosecond TA experiments, they were performed by using a PhaseTech spectrometer (PhaseTech Spectroscopy, Inc.). The Near IR pump pulse (for multi-photon excitation) was generated from an optical parametric amplifier (NDFG, Light Conversion) that was pumped by a 1 kHz regenerative amplifier (Coherent Astrella, 35 fs, 1 kHz, 800 nm), with 3.5 mJ input pulse energy. (For single-photon excitation, the 400 nm pump pulse was produced by the second harmonic generation (SHG) of the 800 nm). The system was seeded by a mode-locked Ti-sapphire oscillator (Coherent Vitesse, 80 MHz). The white light continuum probe beam was generated by focusing a small portion (~10 μ J) of the regenerative amplifier's fundamental 800 nm laser pulses into a 2 mm sapphire crystal (for visible range). The probe beam was collected using a CCD sensor (Teledyne e2v). Steady-state absorption spectra were collected using a Shimadzu UV-3600 UV-VIS-NIR spectrophotometer. PLQY measurements were performed using a Horiba Jobin-Yvon Fluorolog system equipped with iHR320 monochromator, coupled with a photomultiplier tube and a spectrally calibrated Spectralon-coated integrating sphere (Quanta-Phi). Excitation energy was varied by selecting different components of a Xe lamp emission with a monochromator. Dilute solutions of the samples were contained in a 2 mm quartz cuvette.

2. Infrared Pump Pulse Characterization

We applied a simple method to characterize the pulse width information of infrared pump signals.²⁰ The cross-correlation between infrared pump pulse and white light (WL) pulse is reflected by fitting the non-resonant electronic response signal from the pump probe 2D spectrum of sample. The fitting equation is shown as follows:

$$\Delta A = D \cdot \exp\left\{-\frac{[t_d - t_0(\omega)]^2}{\tau_1^2}\right\} \times \sin\left\{\frac{1}{2\beta\tau_1^2} - \frac{[t_d - t_0(\omega)]^2}{\beta\tau_1^4} - \frac{t_0(\omega)[t_d - t_0(\omega)]}{\beta\tau_1^2\tau_2^2}\right\} \quad (1)$$

where D is the amplitude term, t_d is time delay, $t_0(\omega)$ is frequency dependent time zero because of the WL chirp, τ_1 is infrared pump pulse duration, τ_2 and β is WL pulse duration and chirp rate. The cross-correlation signal is detectable even at a low pump fluence of only ~0.06 mJ/cm² (**Figure S4**). The sample's bleach feature first emerges at a pump fluence of roughly 0.3 mJ/cm² (**Figure S1f**), by which the cross-correlation is sufficiently pronounced to allow reliable pulse-width determination. Moreover, for longer-wavelength pumps (corresponding to higher-order multiphoton excitation), the same effect is readily observed and equally suitable and easy for pulse-width analysis. Thus, this *in situ* cross-correlation method provides an ideal, reliable and inherent means to measure pulse duration in our TA method. From the cross-correlation between the certain infrared pump pulse and selected wavelengths in WL pulse, we used global fitting to share τ_1 , estimating the pulse width of 800 nm, 1200 nm, 1700 nm and 2100 nm pulse to be 110 fs, 120 fs, 220 fs and 280 fs (**Figure S5**),

respectively, in which the infrared pump pulse duration increased when the wavelength is shifted to the longer end.

3. Transient Absorption (TA) Spectroscopy Characterization

For single-/multi-photon excited femtosecond TA experiments, we performed by using a PhaseTech spectrometer (PhaseTech Spectroscopy, Inc.). The Near IR pump pulse (for multi-photon excitation) was generated from an optical parametric amplifier (NDFG, Light Conversion) that was pumped by a 1 kHz regenerative amplifier (Coherent Astrella, 35 fs, 1 kHz, 800 nm), with 3.5 mJ input pulse energy. (For single-photon excitation, the 400 nm pump pulse was produced by the second harmonic generation (SHG) of the 800 nm). The system was seeded by a mode-locked Ti-sapphire oscillator (Coherent Vitesse, 80 MHz). The white light continuum probe beam was generated by focusing a small portion (~10 μJ) of the regenerative amplifier's fundamental 800 nm laser pulses into a 2 mm sapphire crystal (for visible range). The probe beam was collected using a CCD sensor (Teledyne e2v). In addition, for 2-photon absorption cross-section measurement of the standard material MAPbBr₃ NCs shown in **Figure S7**, TA spectroscopy was conducted with a modified commercial HELIOS femtosecond transient absorption spectrometer (Ultrafast Systems, LLC). A portion of the 800 nm fundamental output from the regenerative amplifier (Coherent Libra, 1 kHz, 50 fs) was used to pass through an optical parametric amplifier (Coherent OPerA Solo) to get the pump pulse. Another portion of the 800 nm fundamental beam from the regenerative amplifier was focused into a sapphire crystal to generate a broadband visible continuum (400-800 nm) that was used as the probe pulse. The probe beam was passed through a 750 nm short-pass filter to eliminate the residual 800 nm fundamental components and to prevent the strong secondary photoexcitation of the sample. The signals were collected by using a CMOS sensor within the spectrometer. The measured instrument response function of the TA setup was ~160 fs (**Figure S7**), consistent with that reported before²¹. All measurements were conducted at room-temperature conditions. The TA delay curves are fitted with a biexponential function:

$$\Delta A = y_0 + \sum_{i=1}^2 A_i \cdot \frac{1 + \operatorname{erf}\left(\frac{t-t_0}{r} - \frac{r}{2\tau_i}\right)}{2} \cdot \exp\left(-\frac{t-t_0}{\tau_i}\right) \quad (2)$$

where t is the probe delay time, A_i and τ_i are amplitudes of TA and decay lifetimes, respectively. In addition, y_0 is the baseline offset, t_0 is the onset time, r is the rise time constant or instrumental response factor, and $\operatorname{erf}(\cdot)$ is the error function, modelling a gradual transition due to the system response.

References

- 1 Y. Jiang, K. F. Li, K. Gao, H. Lin, H. L. Tam, Y.-Y. Liu, Y. Shu, K.-L. Wong, W.-Y. Lai, K. W. Cheah and W. Huang, *Angew. Chem. Int. Ed.*, 2021, **60**, 10007-10015.
- 2 L. Zhang, M. Morshedi and M. G. Humphrey, *Angew. Chem. Int. Ed.*, 2022, **61**, e202116181.
- 3 Z. Zheng, H. Zhang, H. Cao, J. Gong, M. He, X. Gou, T. Yang, P. Wei, J. Qian, W. Xi and B. Z. Tang, *ACS Nano*, 2022, **16**, 6444-6454.
- 4 S. Wang, X. Li, S. Y. Chong, X. Wang, H. Chen, C. Chen, L. G. Ng, J. W. Wang and B. Liu, *Adv. Mater.*, 2021, **33**, e2007490.
- 5 R. Medishetty, L. Nemeč, V. Nalla, S. Henke, M. Samoc, K. Reuter and R. A. Fischer, *Angew. Chem. Int. Ed.*, 2017, **56**, 14743-14748.
- 6 H. He, Y. Cui, B. Li, B. Wang, C. Jin, J. Yu, L. Yao, Y. Yang, B. Chen and G. Qian, *Adv. Mater.*, 2019, **31**, e1806897.
- 7 W. Chen, S. Bhaumik, S. A. Veldhuis, G. Xing, Q. Xu, M. Grätzel, S. Mhaisalkar, N. Mathews and T. C. Sum, *Nat. Commun.*, 2017, **8**, 15198.
- 8 G. Xing, S. Chakraborty, S. W. Ngiam, Y. Chan and T. C. Sum, *J. Phys. Chem. C*, 2011, **115**, 17711-17716.
- 9 Y. Gao, A. Tonizzo, A. Walser, M. Potasek and R. Dorsinville, *Appl. Phys. Lett.*, 2008, **92**, 033106.
- 10 A. D. Lad, P. Prem Kiran, G. Ravindra Kumar and S. Mahamuni, *Appl. Phys. Lett.*, 2007, **90**, 133113.
- 11 S. Tong, J. Zhong, X. Chen, X. Deng, J. Huang, Y. Zhang, M. Qin, Z. Li, H. Cheng, W. Zhang, L. Zheng, W. Xie, P. Qiu and K. Wang, *ACS Nano*, 2023, **17**, 3686-3695.
- 12 C. A. Leatherdale, W. K. Woo, F. V. Mikulec and M. G. Bawendi, *J. Phys. Chem. B*, 2002, **106**, 7619-7622.
- 13 C. de Mello Donegá and R. Koole, *J. Phys. Chem. C*, 2009, **113**, 6511-6520.
- 14 D. V. Talapin, N. Gaponik, H. Borchert, A. L. Rogach, M. Haase and H. Weller, *J. Phys. Chem. B*, 2002, **106**, 12659-12663.
- 15 I. Moreels, K. Lambert, D. Smeets, D. De Muynck, T. Nollet, J. C. Martins, F. Vanhaecke, A. Vantomme, C. Delerue, G. Allan and Z. Hens, *ACS Nano*, 2009, **3**, 3023-3030.
- 16 J. Li, C. Ren, X. Qiu, X. Lin, R. Chen, C. Yin and T. He, *Photon. Res.*, 2018, **6**, 554-559.
- 17 J. Puthenpurayil, O. H. Cheng, T. Qiao, D. Rossi and D. H. Son, *J. Chem. Phys.*, 2019, **151**, 154706.
- 18 N. S. Makarov, S. Guo, O. Isaienko, W. Liu, I. Robel and V. I. Klimov, *Nano Lett.*, 2016, **16**, 2349-2362.
- 19 L. Protesescu, S. Yakunin, M. I. Bodnarchuk, F. Krieg, R. Caputo, C. H. Hendon, R. X. Yang, A. Walsh and M. V. Kovalenko, *Nano Lett.*, 2015, **15**, 3692-3696.
- 20 M. Feng, S. Ye, J. W. M. Lim, Y. Guo, R. Cai, Q. Zhang, H. He and T. C. Sum, *Small*, 2023, **19**, e2301831.
- 21 J. W. M. Lim, Y. Guo, M. Feng, R. Cai and T. C. Sum, *J. Am. Chem. Soc.*, 2024, **146**, 437-449.